Nanoscale

ROYAL SOCIETY OF CHEMISTRY

COMMUNICATION

View Article Online
View Journal | View Issue

Check for updates

Cite this: *Nanoscale*, 2021, **13**, 6772

Received 13th January 2021,
Accepted 21st March 2021

DOI: 10.1039/d1nr00238d

rsc.li/nanoscale

Engineering conductive protein films through nanoscale self-assembly and gold nanoparticles doping†

Sara H. Mejias, ‡[a,b,c] Elena López-Martínez, ‡[c] Maxence Fernandez, [c] Pierre Couleaud,[a,b] Ana Martin-Lasanta,[a,d] David Romera,[a,b] Ana Sanchez-Iglesias,[c] Santiago Casado,[a] Manuel R. Osorio,[a] Jose M. Abad,[a,e] M. Teresa González *[a] and Aitziber L. Cortajarena *[a,b,c,f]

Protein-based materials are usually considered as insulators, although conductivity has been recently shown in proteins. This fact opens the door to develop new biocompatible conductive materials. While there are emerging efforts in this area, there is an open challenge related to the limited conductivity of protein-based systems. This work shows a novel approach to tune the charge transport properties of protein-based materials by using electron-dense AuNPs. Two strategies are combined in a unique way to generate the conductive solid films: (1) the controlled self-assembly of a protein building block; (2) the templating of AuNPs by the engineered building block. This bottom-up approach allows controlling the structure of the films and the distribution of the AuNPs within, leading to enhanced conductivity. This work illustrates a promising strategy for the development of effective hybrid protein-based bioelectrical materials.

Introduction

Protein-based materials, due to their structural flexibility and their chemical diversity,[1] have brought new opportunities in a wide range of biotechnological and nanotechnological applications, such as tissue regeneration,[2–4] catalysis,[5–7] and plasmonics.[8–10] For example, protein-based nanostructures can be formed with highly tunable properties, including dynamic assemblies.

Moreover, protein-based functional hybrid structures are generated with the specific arrangement of active elements along the protein backbone.[11–16] Recently, proteins have been proposed as candidates for the interfacing of biomolecules with electronic devices due to their intrinsic molecular conduction.[17–19] Long-range electronic conductivity in protein-based materials arises from two mechanisms: (1) redox mediated *via* hopping electron transfer across redox centers, which are spaced closely enough for coherent overlap to occur,[17,20,21] or (2) nonredox-mediated conduction with a band gap, that depends on the protein amino acid composition and the secondary structure of the protein scaffolds.[17,22–25] Protonic conductivity occurs when protons are transported along the protein scaffold by charged amino acids, such as aspartic and glutamic acids.[26–28] In addition, special charge transport occurs between redox active amino acids, such as tyrosine or tryptophan, where the charge transport happens by proton-coupled electron transfer simultaneously showing electronic- and protonic transport.[23,29] These different types of transport can interplay depending on the composition of the material.[30] The control of the charge transport mechanism in protein-based materials would allow tuning their conductive properties, necessary to generate bio-based conductive materials and devices. Several strategies have been reported to boost electronic or protonic charge transport in protein-based systems. For example, protonic charge transport in reflectin protein films has been tuned by varying the composition of the charge amino acids.[26] The electronic transport has been favored by the introduction of redox active amino acids, such as tryptophan or tyrosine, or redox active compounds, such as naphthalene diimide (NDI) along the protein scaffold.[14,31–35] Despite the increasing knowledge on transport mechanisms, charge transport through long distances is difficult to control

[a]*IMDEA Nanociencia, Campus Universitario de Cantoblanco, C\Faraday, 9, 28049 Madrid, Spain. E-mail: teresa.gonzalez@imdea.org*
[b]*Nanobiotechnology Unit (iMdea Nanociencia) associated with Centro Nacional de Biotecnología (CNB-CSIC), Campus Universitario de Cantoblanco, Madrid 28049, Spain*
[c]*Center for Cooperative Research in Biomaterials (CIC biomaGUNE), Basque Research and Technology Alliance (BRTA), Paseo de Miramón 182, 20014 Donostia San Sebastián, Spain. E-mail: alcortajarena@cicbiomagune.es*
[d]*Departamento de Química Orgánica, Universidad de Granada, Campus Fuentenueva s/n, E-18071 Granada, Spain*
[e]*Departamento de Química Analítica y Análisis Instrumental, Facultad de Ciencias, Universidad Autónoma de Madrid, 28049 Madrid, Spain*
[f]*Ikerbasque, Basque Foundation for Science, Mª Díaz de Haro 3, 48013 Bilbao, Spain*
†Electronic supplementary information (ESI) available: Figure. See DOI: 10.1039/d1nr00238d
‡These authors contributed equally to this work.

and tune as it depends on the structure of the material and its chemical composition.[17,18,30,36]

The current work describes a novel approach that combines protein design, biomolecular templating of gold nanoparticles (AuNPs), and protein self-assembly to enhance the conductive properties of protein-based films (Fig. 1). The consensus tetratricopeptide repeat protein (CTPR) used as protein scaffold is made of a 34 amino acid helix-turn-helix module.[37,38] The fold of CTPRs is defined by a few conserved residues; hence, there is a lot of room for engineering non-conserved amino acids.[37] The modules generally appear in tandem repeats, from 2 to 20, generating a rigid right-handed superhelical structure.[37] CTPRs assemble forming a transparent ordered solid film through their intrinsic self-assembly properties of the structured units.[37,39] As previously demonstrated, these self-assembly capabilities enable the fabrication of photoconductive and electroactive functional assemblies based on CTPRs.[11,40] CTPR protein-based films have shown protonic transport due to their ionic nature and high content of charged amino acids, and as such have been proven to be interesting actuators that respond to humidity in the environment.[41] In parallel works, the incorporation of AuNPs for electrical interfacing of redox enzymes, or the AuNP-assisted assembly of heme protein resulted in effective improvement of the long-range charge transfer efficiency.[42–44] AuNPs have been also used to generate AuNPs-peptide conductive nanocomposites.[45] The aforementioned works show the value of design strategies to improve conductivity in protein-based systems, and inspired the use of AuNPs as electron conductive elements in a CTPR-based macroscopic hybrid films.

Herein, a CTPR unit was first designed to template AuNPs with nanometer precision through an orthogonal conjugation strategy. Then, protein self-assembly after solvent evaporation guided the formation of both solid films of CTPRs and CTPR-AuNPs.[39] Remarkably, the CTPR films already displayed conductivity in the hundred nS/m range, recordable at micrometer length scales and mainly attributed to protonic charge transport. The CTPR-AuNPs hybrid films showed an enhancement of four orders of magnitude in conductivity when compared to the CTPR-only films, and, presumably, different charge transport properties. The current results demonstrate a strategy to fabricate protein-based conductive films with enhanced conductivity by using highly conductive nano-elements, which paves the way for future application of hybrid protein-based systems in the field of bioelectronics.

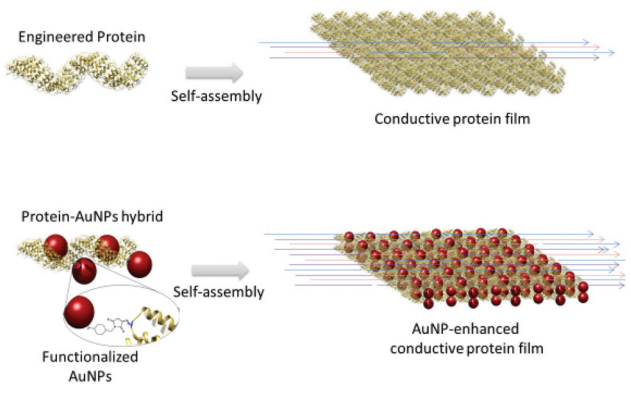

Fig. 1 Conductive protein-based biomaterials. Top. Engineered repeat proteins as building blocks to fabricate self-assembled conductive films. Bottom. Protein-AuNPs hybrids as building blocks to fabricate AuNPs-doped self-assembled films with enhanced conductivity.

Experimental

Materials

All chemical reagents were purchased from Aldrich and used without further purification. Ultrafiltration tubes used were Amicon Millipore with a regenerated cellulose membrane and a cut-off of 3 kDa. Cobalt NTA affinity resin used is ABT 6BCL-QHCo-100 (Agarose Bead Technology). Ultrapure reagent grade water (18.2 MΩ, Wasserlab at 25 °C) was used in all experiments. Gold(III) chloride hydrate ($HAuCl_4$, ≥99%), sodium citrate tribasic dihydrate (≥98%), sodium borohydride ($NaBH_4$, ≥96%) and mercapto poly (ethylene glycol) amine functionalized (HS-PEG2K-NH_2) were purchased from Sigma-Aldrich-Merck. All glassware was washed with aqua regia, rinsed with Milli-Q water, and dried before use.

Measurements

UV-Vis and fluorescence spectra were recorded on a Synergy H4 microplate reader (BioTek) using 96-well plates. Fast Protein Liquid Chromatography (FPLC) was performed on a GE Life Science ÄKTA prime plus apparatus with a Superdex 75 column. Gel reader apparatus used was a Syngene G:Box Chemi XR5. Matrix Assisted Laser Desorption/Ionization Time Of Flight mass spectrometry (MALDI-TOF) was done by the National Center of Biotechnology (CNB) proteomic service in Madrid on an AB Sciex ABi 4800 MALDI TOF/TOF mass spectrometer. High Resolution Transmission Electronic Microscopy (HR-TEM) measurements were done on a JEOL JEM 1400 Plus.

Gel filtration chromatography

Gel filtration chromatography was performed using an AKTA prime plus Fast Protein Liquid Chromatography (FPLC) equipment (GE Healthcare). After Ni-NTA column purification, the dialyzed elution fractions were injected into a Superdex 75 HR 10/30 size exclusion chromatography column (GE Healthcare) and run at 0.5 mL min^{-1} in PBS buffer with a detection UV absorption at 280 nm. The samples were collected in 0.5 mL fractions and stored at 4 °C.

High resolution transmission electron microscopy (HR-TEM)

HR-TEM measurements were conducted on JEOL JEM 1400 Plus microscope. The samples for HR-TEM were prepared by drop contact of the sample solution at 100 nM concentration of protein with a TEM grid and blotted to dry. The analysis of the images was performed using ImageJ software. The statisti-

cal analysis was performed using a Mann–Whitney non parametrical test with GraphPad Prism software.

Scanning tunnel microscopy (STM)

STM images were obtained with a home-built Scanning Tunnelling Microscope designed for room-temperature experiments.[46] All the images were recorded in ambient conditions using commercial gold substrates (Arrandee) cleaned prior sample deposition by flame-annealing. Freshly cut gold wires (99.99%) were used as tips. Samples were prepared by the drop casting technique from an aqueous solution of $CTPR16_{4Cys}$-AuNPs. For individual molecule imaging, we used 0.1–10 nM concentrations, while for layer formation, we used a 1 μM protein concentration. A drop of 200–300 μL of the solution was deposited over our 1 cm^2 gold substrates, which were rinsed with water several times after assembly periods of 10 to 30 minutes. The gold surface was then dried under N_2 flow. Images were recorded using bias voltage values between 0.1 V and 1.5 V and a setpoint current between 500 pA and 5 nA. The body of the protein could not be imaged in range of voltages studied reflecting its low electrical conductance. The typical apparent height of the AuNP was 0.4 nm, accounting for their expected poor coupling to the gold substrate.

X-ray diffraction (XRD)

XRD was performed in a Panalytical X'Pert PRO diffractometer with Cu tube (lambda Kα = 1.54187 Å) operated at 45 kV, 40 mA, Ni beta filter, programmable divergence and antiscatter slits working in fixed mode, and fast linear detector (X'Celerator) working in scanning mode.

Gold nanoparticles synthesis

Gold nanoparticles (~3 nm) were prepared by fast reduction of $HAuCl_4$ (20 mL, 0.125 mM) with freshly prepared $NaBH_4$ (0.3 mL, 10 mM) in the presence of sodium citrate (0.25 mM) under vigorous stirring.[47] The solution color changed from yellow to reddish. After two minutes, the seed solution was aged at 27 °C for 30 min before use to promote the decomposition of sodium borohydride. Mercapto poly (ethylene glycol) amine functionalized with a molecular weight of 2000 g mol^{-1} was used for ligand exchange. An aqueous solution of HS-PEG2K-NH_2 (0.5 mL, 2.9 mM) was added dropwise to as synthesized gold nanoparticles under vigorous stirring. The mixture was allowed to react for 2 h. PEG-modified gold nanoparticles were centrifuged using Millipore Amicon Centrifugal Filter Units (10 kDa) and finally dispersed in water.

Protein design and purification

Based on consensus CTPR16 protein, four cysteine residues were introduced in a loop position 33 of the CTPR repeats 2, 6, 10, and 14 to form $CTPR16_{4Cys}$ protein. The mutation was introduced in CTPR1 by quick-change site directed mutagenesis. The $CTPR16_{4Cys}$ gene was generated from the CTPR1 wild type gene by sequential additions of CTPR1 wild type or mutated repeats, depending on the CTPR repetition number, and cloned into pPro-EX-HTa vector. The protein was expressed as His-tagged fusion and purified using standard affinity chromatography methods as previously described.[48] The protein was dialyzed into PBS buffer (150 mM NaCl, 50 mM phosphate buffer pH 7.4) with 2 mM β-mercaptoethanol and stored frozen at −20 °C. The protein concentration was determined by UV-absorbance at 280 nm using the extinction coefficient calculated from the amino acid composition.[49]

Modification of AuNPs and conjugation with $CTPR16_{4Cys}$ protein

1 mL of amine-PEG AuNPs at 160 nM were incubated with 39 μL of freshly prepared 22.9 μM 4-(*N*-maleimidomethyl) cyclohexane-1-carboxylic acid 3-sulfo-*N*-hydroxysuccinimide ester dissolved in water (Sulfo-SMCC) in a microtube for 30 min at room temperature (final molar ratio Sulfo-SMCC : AuNPs = 5 : 1). The AuNPs concentration was calculated from their absorption at 510 nm using the following equation: $\ln \varepsilon = 3.32111 \times \ln D + 10.80505$, where ε is the molar extinction coefficient (M^{-1} cm^{-1}) and D is the nanoparticle core diameter in nm of the gold nanoparticles measured by TEM, according to Liu *et al.*[50] Protein cysteines were reduced using 5 mM dithiothreitol (DTT) for 45 minutes and purified using an Illustra NAP-5 desalting column equilibrated with a solution of 150 mM NaCl, 50 mM phosphate buffer pH 8.0. Before conjugation, the excess Sulfo-SMCC was removed from the AuNPs suspension by using an ultrafiltration unit Amicon® Ultra – 0.5 mL with a 3000 Da molecular weight cutoff (MWCO) at 21 000 g for 5 min and by washing 5 times with 150 mM NaCl, 50 mM phosphate buffer pH 8.0. Purified AuNPs-SMCC were then incubated with 7.6 μL of 5.9 μM freshly reduced $CTPR16_{4Cys}$ at room temperature with 20 rpm spinning for 1 h (final molar ratio $CTPR16_{4Cys}$:AuNPs = 1 : 4). After nanoparticle conjugation, the reaction was blocked by the addition of 5 μL of 10 mM β-mercaptoethanol. After overnight incubation, $CTPR16_{4Cys}$-AuNPs conjugates were purified from the excess of unbound AuNPs and linker using protein His-Tag and Ni-NTA column. Free AuNPs were eluted in the flow-through while $CTPR16_{4Cys}$-AuNPs conjugate was eluted from the nickel column with a 300 mM imidazole buffer solution.

Film formation

Protein solid ordered films were generated as previously described.[51] $CTPR16_{4Cys}$ protein alone and $CTPR16_{4Cys}$-AuNPs conjugates were diluted to 3% (w/v) protein concentration in 10 mM NaCl, 10 mM Na phosphate pH 7.0 buffer. The solutions were deposited on different surfaces, depending on the experiments to be performed. Quartz cuvette was used for circular dichroism (CD) analysis, glass surface for conductivity measurements and silicon wafer for X-ray diffraction (XRD) analysis. The drop volumes also vary between 10 to 30 μL. The solvent was evaporated at room temperature for 12 hours, resulting in solid thin films.

Lithography of the electrodes

A pattern of interdigitated electrodes with a defined channel of 20 μm in length L and 11.8 mm in width W was fabricated

through clean-room processes of "maskless" lithography ("Heidelberg DWL66fs" model) and thermal evaporation. A Si/SiO_2 wafer was coated by 2 mm "AZ 1512HS" (MicroChemicals GmbH) positive resin and exposed to a λ = 405 nm laser that printed the designed electrode pattern. The wafer was then introduced in a AZ351B developer (1 : 4 developer:water) to remove the resin parts exposed to the laser. To ensure that all the resin is removed, the wafer was further exposed to plasma (50 W) for 30 s. The revealed sample was introduced in a thermal evaporator (Nanosphere, de Oxford Vaccum Science model) where a chromium 5–10 nm thick layer was first evaporated to increase the adhesion to the substrate, followed by a 50 nm thick gold layer. To finish, a lift-off process was performed, introducing the sample in acetone to remove all the resin in the sample and obtain the desired pattern shown in Fig. S1.†

Electrical conductivity measurements

To study the conductive properties of the $CTPR16_{4Cys}$ and $CTPR6_{4Cys}$-AuNPs, we prepared thin films of the protein and the conjugate devices over silicon wafers with gold electrodes patterned as described in the previous section (Fig. S1†). Using a Keithley 4200-SCS, we recorded current *versus* voltage curves in the interval (−1 V, +1 V) for both the $CTPR16_{4Cys}$ protein and the $CTPR16_{4Cys}$-AuNPs conjugate. Olympus standard silicon nitride probes of 0.05 N m^{-1} and 18 kHz (OMCL-RC800PSA) were employed to contact the electrodes. The aspect ratio (W/L) of the interdigitated electrodes is 590, which allowed us to obtain measurable currents even for low-conducting plain $CTPR16_{4Cys}$ films, and to reduce the effect of edge currents between the electrodes. Due to the low conductance of the $CTPR16_{4Cys}$, we prepared thicker film of this protein than of the AuNP conjugate. We prepared 4–5 μm thick films for the protein, and 20–100 nm thick films for the conjugate. The thickness of the films was measured using a profilomer for CTPR16 films and an atomic force microscope (AFM) in jumping mode for the $CTPR16_{4Cys}$-AuNPs films.

Results

CTPR proteins were identified as good candidates to generate protein-based conductive films, due to their ability to form ordered macroscopic materials through their self-assembly properties. CTPR16, a protein composed of sixteen CTPR repeats, was chosen as scaffold considering its high stability and its 16 nm length which makes it suitable for templating several nanoparticles per protein. Moreover, as it has been demonstrated for squid ring teeth proteins, the number of tandem repetitions significantly and systematically enhances bulk transport properties.[52] Therefore, sixteen CTPR repeats appeared as an appropriate protein size for promoting conductivity. To ensure a homogeneous and controlled distribution of AuNPs over the CTPR film, AuNPs were precisely introduced on selected regions of the CTPR scaffold by covalent linkage. CTPR16 protein was engineered with 4 unique cysteine residues in the loop of the 2nd, 6th, 10th, and 14th repeats, by the mutation R33C for the selective conjugation of the AuNPs, leading to $CTPR16_{4Cys}$ (Fig. 2A). Position 33 within the CTPR sequence was selected since it is a non-conserved position[53] and therefore a non-structural position, and it is located in a solvent exposed loop that will facilitate the conjugation. Repeats 2nd 6th, 10th and 14th were selected to encode a CTPR-AuNP complex with optimal inter-particle distance with 2 nanoparticles per superhelical turn[54] and alternate particles facing opposite sides of the superhelix (Fig. 2A and S2†). These mutations did not significantly affect the structure or the stability of the scaffold, as confirmed by circular dichroism (CD) (Fig. 2B). The synthesized AuNPs functionalized with amine-polyethylene glycol (PEG) coating had an average diameter of 3.1 ± 0.7 nm and their colloidal stability is maintained by the PEG monolayer (see Experimental for details). These AuNPs showed a localized surface plasmon resonance (LSPR) around 510 nm.

Amine-PEG AuNP were conjugated to $CTPR16_{4Cys}$ proteins using sulfo-SMCC conjugation chemistry. As show in Fig. 2C, the NHS ester group of the sulfo-SMCC linker reacts with amine groups of the amine-PEG AuNPs while its maleimide group reacts orthogonally with the cysteines in the protein

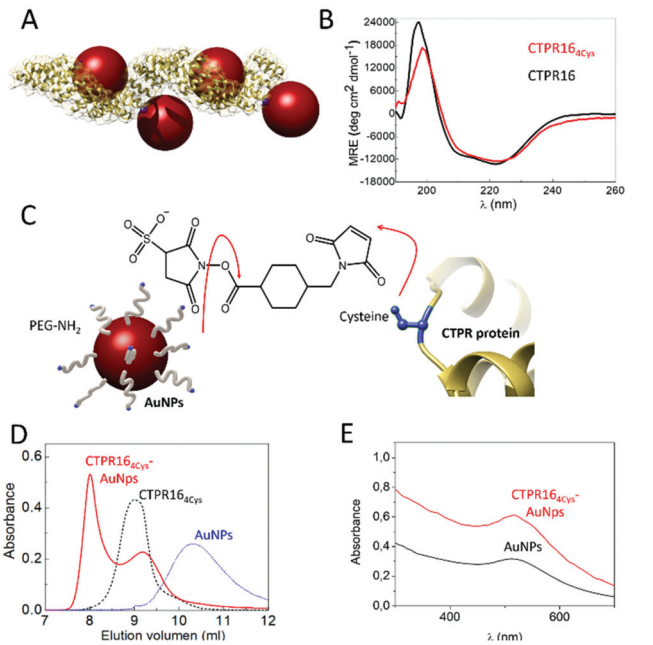

Fig. 2 (A) Ribbon representation of the $CTPR16_{4Cys}$-AuNPs conjugated protein. Structural model is based on the structure of PDB ID: 2HYZ. The mutated cysteine residues are highlighted in blue. (B) CD spectra of $CTPR16_{4Cys}$ (red line) compared with the original CTPR16 (black line). (C) Schematic representation of the conjugation strategy followed. The free amines from the PEGylated AuNPs and the thiol groups from the cysteines (shown in blue) of the $CTPR16_{4Cys}$ protein are linked using sulfo-SMCC molecules. (D) Size exclusion chromatograms of AuNPs (blue dotted line), the $CTPR16_{4cys}$ protein (black dotted line) and the $CTPR16_{4cys}$-AuNPs conjugates (red line). (E) UV-Visible spectra of the AuNPs with their characteristic LSPR peak at 520 nm (black line) and the $CTPR16_{4cys}$-AuNPs conjugate (red line).

scaffold. After conjugation, the CTPR16$_{4Cys}$-AuNPs complexes were purified from unbound AuNPs by affinity chromatography. The eluate that exhibited a pink/purple color, characteristic of the AuNPs, was analyzed by size exclusion chromatography (Fig. 2D). The elution time for the CTPR16$_{4Cys}$-AuNPs was the shortest, which confirmed AuNPs incorporation to the CTPR16$_{4Cys}$ that resulted in a larger hydrodynamic radius compared to CTPR16$_{4Cys}$, and to the AuNPs. Moreover, the UV-visible absorption spectrum of the CTPR16$_{4Cys}$-AuNPs conjugates showed the AuNPs LSPR peak at 510 nm (Fig. 2E).

The conjugation efficiency was analyzed by transmission electron microscopy (TEM) (Fig. 3A). TEM images were acquired and the distribution of the AuNPs showed the presence of spatially limited assemblies made of 3 or 4 particles, with a disposition in agreement with the arrangement encoded by the engineered CTPR16$_{4Cys}$ scaffold (Fig. 3A, left panel). Such assembled nanostructures were not observed in the original amine-PEG functionalized AuNPs, for which mostly large aggregates of particles are observed (Fig. 3A, right panel). The CTPR16$_{4Cys}$-AuNPs conjugates also revealed some larger assemblies composed of more than 4 AuNPs per groups, which could be due to the linkage of two or more proteins through the AuNPs, as the activated AuNP-SMCC intermediates are not monovalent and could potentially be grafted by two or more proteins. However, the conjugates assemblies and the control-particle before conjugation show different behavior, with predominance of 1–4 assemblies in the conjugates, whereas predominance of large nonspecific aggregates in the control (Fig. S3†).

The CTPR16$_{4Cys}$-AuNPs nanoscale structure was explored using scanning tunneling microscopy (STM) at bias voltages between 0.1 V and 1.5 V and at room temperature (Fig. 3B). Conjugated CTPR16$_{4Cys}$-AuNPs at 1 nM were deposited by drop casting over a freshly flame-annealed gold surface (see Experimental for details). Groups of four AuNPs disposed in good agreement with the disposition of the four cysteine residues in the designed protein were observed. According to image profiles, the distances between gold nanoparticles are slightly larger than expected from the model based on CTPR crystal structure, which can be explained by the flexibility of the CTPR spring-like backbone.[55] Moreover, since STM images are based on the current measured between the tip and the sample, the obtained STM images already confirm the conductivity of the AuNPs attached to the scaffold protein.

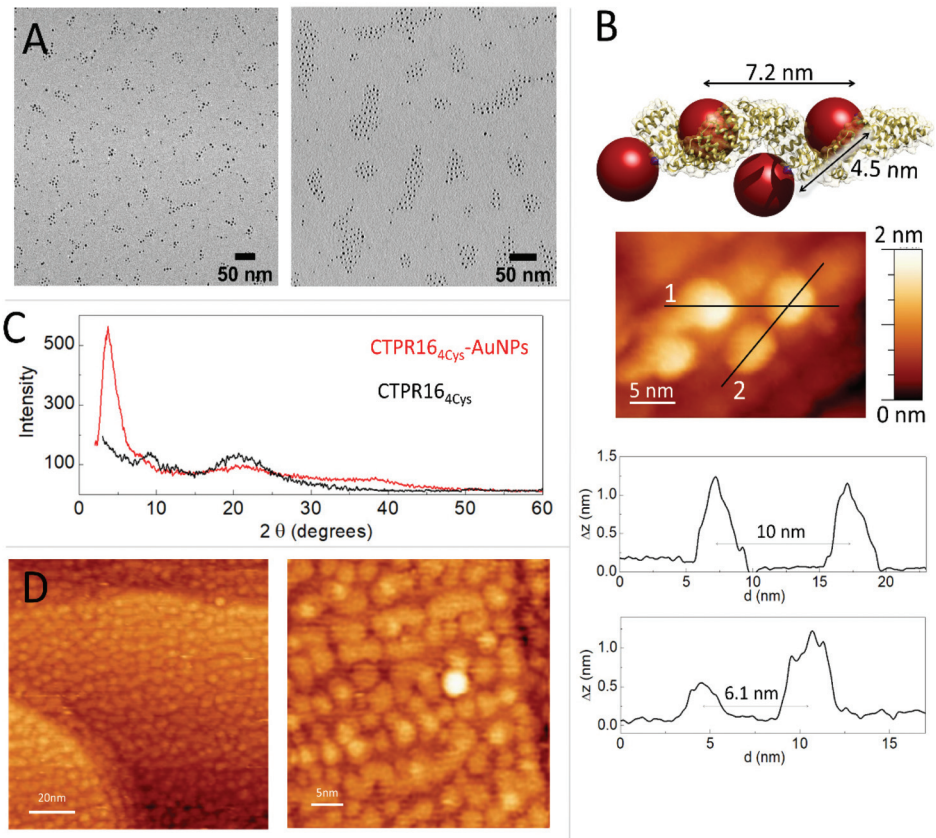

Fig. 3 (A) Left: TEM micrograph of CTPR16$_{4Cys}$-AuNPs conjugates in discrete groups. Right: TEM micrograph of the PEGylated AuNPs in aggregates. (B) Model structure of CTPR16$_{4Cys}$-AuNPs conjugate based on the crystal structure of CTPR20 and the location of the cysteine mutations in the CTPR protein. A STM image of one CTPR16$_{4Cys}$-AuNPs conjugate is shown with the profile plots of lines 1 and 2 shown below (profile for line 1 on top, and profile for line2 on bottom). (C) Powder X-ray Diffraction (P-XRD) spectra of CTPR16$_{4Cys}$-AuNPs conjugate film in red and P-XRD spectra of the CTPR16 film in black. (D) STM images of the CTPR16$_{4cys}$-AuNPs conjugates deposited on a gold surface at different magnifications.

CTPR16$_{4Cys}$ and CTPR16$_{4Cys}$-AuNPs solid state assemblies were generated taking advantage of CTPR protein intrinsic interactions.[39] A 300 μM protein solution was deposited into a planar surface and a transparent solid film was formed after drop drying. X-ray diffraction (XRD) was used to check internal order in the films (Fig. 2C). The XRD spectrum of the CTPR16$_{4Cys}$ film showed two peaks at 2θ = 9.6° (001) and 20.0° (002) which could correspond to a lamellar packing of the protein with a periodical *d*-spacing of 9.1 Å, in agreement with previously described CTPR protein films.[11] CTPR16$_{4Cys}$-AuNPs films also showed a peak at 2θ = 20.1°, related to the protein packing. In addition, these AuNPs-doped films exhibited two peaks which are not present in the pure protein film. A first peak at 2θ = 37.7° assigned to the crystal structure of AuNPs[56] and a second peak at 2θ = 3.6° which corresponds to a periodical *d*-spacing of 2.3 nm. This spacing is attributed to the arrangement of gold nanoparticles within the solid film. It suggests a tighter packing of the AuNPs in the 3D film than the one observed by STM in a single molecule arrangement (Fig. 3B). To explore further the packing of the gold nanoparticles within the CTPR16$_{4Cys}$-AuNPs films, STM was performed (Fig. 3D). A 1 μM solution of CTPR16$_{4Cys}$-AuNPs conjugates (1000 times higher than the previous concentration for single molecule imaging) was deposited directly onto a gold surface. After solvent evaporation, a thin layer of CTPR16$_{4Cys}$-AuNPs was formed. STM images of the formed layer showed rows of AuNPs homogeneously distributed within the film. AuNPs are closer than expected from linear protein packing, as the proteins intercrossed minimizing AuNPs distances. The average inter-particle distance between AuNPs centers in the film is 4.2 ± 0.3 nm (Fig. 3D) with a nanoparticle gap of ~ 0.6 nm. This smaller interparticle distance measured in the 2D film arrangement when compared with the inter-particle distance determined for individual CTPR16$_{4Cys}$-AuNPs (Fig. 3B), is in agreement with the tighter packing in the solid film previously determined by XRD (Fig. 3C). However, the inter-particle distance in film reported by XRD (2.3 nm) and by STM (4.2 nm) slightly differ since XRD reports on 3D arrangement and STM on 2D.

Charge transport properties of both CTPR16 protein and CTPR16$_{4Cys}$-AuNPs conjugate films were studied by measuring current–voltage (*I–V*) curves in the (−1 V, +1 V) interval (Fig. 4). The absolute value of the applied bias was limited to 1 V, which is smaller than thermoneutral voltage for water electrolysis.[57] Films were formed onto Si/SiO$_2$ wafers with interdigitated gold electrodes on top using different protein and conjugate batches to ensure reproducibility. The electrodes described a channel with a width *W* to length *L* ratio (*W*/*L*) of approximately 600, which minimized the effect of edge currents between the electrodes (see Experimental for details). At low applied voltage, (−0.3 V, 0.3 V) interval, films showed an ohmic behavior (constant *G* in Fig. 4B). In this range, protein films showed an average conductivity value of 140 ± 19 nS m^{-1}, where current was transported through 20 μm of protein film according to the inter-distance length (*L*) between the electrodes. Conductivity was calculated using the equation $\sigma = G \times L/(t \times W)$, where $G = I/V$ is the conductance obtained from the *I–V* curve slope. The thickness of each film (*t*) was measured by atomic force microscopy (AFM) and *W* and *L* were defined by the electrode design (*vide supra*). In the case of the films doped with AuNPs, their conductivity increased by 4 orders of magnitude, with an average value of 1.37 ± 0.35 mS m^{-1} in the same applied voltage range. Measurements were performed across sets of independent batches of proteins and AuNP conjugates with high reproducibility of the current measurements when scaling the results by the film thickness (different curves in Fig. 4A). To better compare the profile of the curves, Fig. 4B shows the voltage dependence of the conductance normalized by its value in the low voltage regime (G/G_{low}). The G/G_{low}-V curves are symmetrical for both the CTPR16$_{4Cys}$ and CTPR16$_{4Cys}$-AuNPs films. The conductance in the CTPR16$_{4Cys}$ films showed a significant increase with the applied voltage, different from the behavior observed for CTPR16$_{4Cys}$-AuNPs films. Assuming that the edge resistivity is similar in the electrodes for all the films, these differences in the curve profile indicate differences in the main charge transport mechanism between the films with and without AuNPs. The normalized conductance of the CTPR16$_{4Cys}$ films showed an exponential increase at absolute values of voltage ≥0.4 V. This non-linear profile is consistent with the presence of charge-carrier blocking at the electrical contacts, which is characteristic of protonic conductivity.[27,41] This observation is in agreement with previously reported protonic charge transport for CTPR protein films.[41] On the contrary, the CTPR16$_{4Cys}$-AuNPs films showed a quasi-linear increase in conductance for most of the explored voltage range (−1 V, 1 V), indicating a difference in their charge transport properties. The enhancement of the conductivity observed for the films with AuNPs is consistent with electron-like charge transport within the films. The inter-particle distance measured in the AuNP-doped films is compatible with hopping electron transfer between the AuNPs,[58,59] in addition the described packing distance between consecutive layers within the protein films[51,60] is also compatible with hopping electron transfer between layers. These effects would facilitate

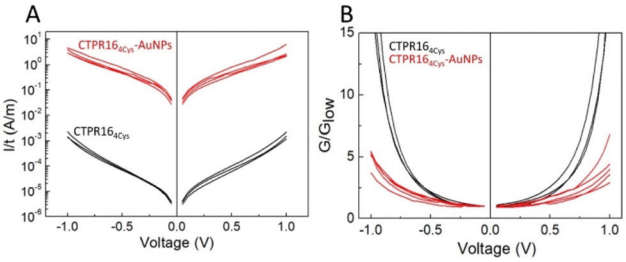

Fig. 4 Transport properties of protein and protein-AuNPs thin films. (A) Current intensity(I) vs applied voltage(V) plot obtained for different CTPR16 films in black and CTPR16$_{4Cys}$-AuNPs films in red. The *Y* axis shows the intensity scaled by the film thickness (*t*) in logarithmic scale. (B) Normalized conductance (G/G_{low}) *vs.* applied voltage(V) for CTPR16 films in black and CTPR16$_{4Cys}$-AuNPs film in red obtained from the curves of part A.

electron transport, thus increasing the conductivity along the CTPR16$_{4Cys}$-AuNPs films. This hypothesis is in agreement with the observations extracted from the G/G_{low} *vs.* V curves. A precise characterization of the charge transport mechanism through the protein films with and without AuNPs would require deeper studies combining several techniques and an analysis of the temperature and humidity dependence of the conductivity. However, the overall results shown here point to a mainly protonic charge transport in the CTPRs films and the emergence of electronic charge transport in the CTPR16$_{4Cys}$-AuNPs films.

Conclusions

This work showed for the first time that gold nanoparticles, as an added electronic component, can be used to enhance the conductivity of protein-based films composed of engineered proteins. The main assets of this approach exploit (i) the rigid superhelical scaffold of CTPR proteins, (ii) their self-assembly properties that makes it possible to form protein films and (iii) the engineering of such proteins to form nanobioconjugates, enabling a strategy for controlled nanoparticles templating.

Our study shows that a rigid superhelical scaffold, *i.e.* the engineered CTPR protein, can be used to regularly space up to 4 AuNPs per protein. Solid protein films were then formed, based on the self-assembly properties of CTPR proteins. Such films formed with pure protein or CTPR16$_{4Cys}$-AuNP conjugates exhibit long-range conductivity. CTPR16$_{4Cys}$-AuNPs films display a conductivity value of 1.37 ± 0.35 mS m^{-1}, four orders of magnitude larger than the one measured for protein films. Furthermore, AuNPs seem to promote a change in the charge transport properties, as reflected by differences in the *I–V* curve profiles. The results presented are consistent with different charge transfer mechanisms: a mainly protonic mechanism for the CTPR films and an additional electronic component for the AuNPs-doped films. The latter favored by the short AuNP inter-particle gap observed in the CTPR16$_{4Cys}$-AuNPs films (~0.6 nm), which is suitable for hopping electron transfer between AuNPs within the films. Although the conductive mechanisms along CTPR and CTPR16$_{4Cys}$-AuNPs films need further studies, our work opens the way to new designs and understandings of long-range conductivity through protein, which is both fundamentally interesting and potentially significant for the development of bioelectronics materials. We also demonstrate a generic approach for grafting any kind of nanoparticle on the scaffold of the proteins without altering its structure. Given the modular nature and the geometry of CTPR proteins, other inorganic nanomaterials could be arranged with adjustable inter-particle distances, making our approach a versatile tool for other applications such as optical coupling.

Author contributions

Conceptualization, A.L.C, and S.H.M.; Methodology, S.H.M., E. L-M, P.C., A.M-L., D.R., M.F., A.S-I, S.C., M.R.O, J.M.A, M.T.G.; Formal analysis, S.H.M., M.F., S.C., J.M.A, M.T.G., and A.L.C; Investigation: protein–nanoparticle conjugation and characterization, S.H.M., E.L-M, P.C., D.R., and M.F.; Investigation: nanoparticle synthesis, J.M.A., A.S-I.; Investigation: STM studies, A.M-L., and M.T.G.; Investigation: conductivity studies, S.H.M., S.C., M.R.O, and, M.T.G; Writing—original draft preparation, S.H.M., E-L.M, J.M.A., M.T.G., and A.L.C.; Funding acquisition, J.M.A., M.T.G., and A.L.C. All authors have read and agreed to the published version of the manuscript.

Conflicts of interest

There are no conflicts to declare.

Acknowledgements

This work was partially supported by the European Research Council ERC-CoG-648071-ProNANO, ERC-PoC-841063-NIMM, Agencia Estatal de Investigación, Spain (PID2019-111649RB-I00; and MAT2017-88693-R), and the Basque Government (Elkartek KK-2017/00008), E.L-M thanks the Spanish Ministry of Science and Innovation for the FPI grant (BES-2017-079646). This work was performed under the Maria de Maeztu Units of Excellence Program from the Spanish State Research Agency – Grant No. MDM-2017-0720 (CIC biomaGUNE) and SEV-2016-0686 (IMDEA Nanociencia).

Notes and references

1 J. Clarke and L. Regan, *Curr. Opin. Struct. Biol.*, 2010, **20**, 480–481.
2 S. Gomes, I. B. Leonor, J. F. Mano, R. L. Reis and D. L. Kaplan, *Prog. Polym. Sci.*, 2012, **37**, 1–17.
3 L. Quintanilla-Sierra, C. García-Arévalo and J. C. Rodriguez-Cabello, *Mater. Today Bio.*, 2019, **2**, 100007.
4 J. Teßmar, F. Brandl and A. Göpferich, in *Fundamentals of Tissue Engineering and Regenerative Medicine*, ed. U. Meyer, J. Handschel, H. P. Wiesmann and T. Meyer, Springer, Berlin, Heidelberg, 2009, pp. 495–517.
5 S. B. J. Kan, X. Huang, Y. Gumulya, K. Chen and F. H. Arnold, *Nature*, 2017, **552**, 132–136.
6 D. W. Watkins, J. M. X. Jenkins, K. J. Grayson, N. Wood, J. W. Steventon, K. K. Le Vay, M. I. Goodwin, A. S. Mullen, H. J. Bailey, M. P. Crump, F. MacMillan, A. J. Mulholland, G. Cameron, R. B. Sessions, S. Mann and J. L. R. Anderson, *Nat. Commun.*, 2017, **8**, 358.
7 A. E. Donnelly, G. S. Murphy, K. M. Digianantonio and M. H. Hecht, *Nat. Chem. Biol.*, 2018, **14**, 253–255.
8 D. Etezadi, J. B. Warner Iv, F. S. Ruggeri, G. Dietler, H. A. Lashuel and H. Altug, *Light: Sci. Appl.*, 2017, **6**, e17029–e17029.
9 E. Ferreira de Macedo, D. M. Ducatti Formaggio, N. Salles Santos and D. Batista Tada, *Sensors*, 2017, **17**, 2765.

10 S. H. Mejias, P. Couleaud, S. Casado, D. Granados, M. A. Garcia, J. M. Abad and A. L. Cortajarena, *Colloids Surf., B*, 2016, **141**, 93–101.
11 S. H. Mejías, J. López-Andarias, T. Sakurai, S. Yoneda, K. P. Erazo, S. Seki, C. Atienza, N. Martín and A. L. Cortajarena, *Chem. Sci.*, 2016, **7**, 4842–4847.
12 P. Couleaud, S. Adan-Bermudez, A. Aires, S. H. Mejías, B. Sot, A. Somoza and A. L. Cortajarena, *Biomacromolecules*, 2015, **16**, 3836–3844.
13 S. H. Mejias, A. Aires, P. Couleaud and A. L. Cortajarena, *Adv. Exp. Med. Biol.*, 2016, **940**, 61–81.
14 J. Zhang, K. Zhou, Y. Zhang, M. Du and Q. Wang, *Adv. Mater.*, 2019, **31**, 1901485.
15 S. Behrens, W. Habicht, K. Wagner and E. Unger, *Adv. Mater.*, 2006, **18**, 284–289.
16 C.-L. Chen, P. Zhang and N. L. Rosi, *J. Am. Chem. Soc.*, 2008, **130**, 13555–13557.
17 N. L. Ing, M. Y. El-Naggar and A. I. Hochbaum, *J. Phys. Chem. B*, 2018, **122**, 10403–10423.
18 I. Ron, I. Pecht, M. Sheves and D. Cahen, *Acc. Chem. Res.*, 2010, **43**, 945–953.
19 V. V. Ptushenko, *Biochemistry*, 2020, **85**, 955–965.
20 H. B. Gray and J. R. Winkler, *Proc. Natl. Acad. Sci. U. S. A.*, 2005, **102**, 3534–3539.
21 M. Cordes and B. Giese, *Chem. Soc. Rev.*, 2009, **38**, 892–901.
22 J. R. Winkler and H. B. Gray, *J. Am. Chem. Soc.*, 2014, **136**, 2930–2939.
23 H. B. Gray and J. R. Winkler, *Q. Rev. Biophys.*, 2003, **36**, 341–372.
24 S. S. Skourtis, I. A. Balabin, T. Kawatsu and D. N. Beratan, *Proc. Natl. Acad. Sci. U. S. A.*, 2005, **102**, 3552–3557.
25 J. Blumberger, *Chem. Rev.*, 2015, **115**, 11191–11238.
26 D. D. Ordinario, L. Phan, W. G. W. Iv, J.-M. Jocson, E. Karshalev, N. Hüsken and A. A. Gorodetsky, *Nat. Chem.*, 2014, **6**, 596–602.
27 L. Glasser, *Chem. Rev.*, 1975, **75**, 21–65.
28 O. Silberbush, M. Amit, S. Roy and N. Ashkenasy, *Adv. Funct. Mater.*, 2017, **27**, 1604624.
29 S. Y. Reece and D. G. Nocera, *Annu. Rev. Biochem.*, 2009, **78**, 673–699.
30 M. Amit, S. Appel, R. Cohen, G. Cheng, I. W. Hamley and N. Ashkenasy, *Adv. Funct. Mater.*, 2014, **24**, 5873–5880.
31 P. Carloni, W. Andreoni and M. Parrinello, *Phys. Rev. Lett.*, 1997, **79**, 761–764.
32 R. A. Jishi, N. C. Braier, C. T. White and J. W. Mintmire, *Phys. Rev. B: Condens. Matter Mater. Phys.*, 1998, **58**, R16009–R16011.
33 J. S. Lee, I. Yoon, J. Kim, H. Ihee, B. Kim and C. B. Park, *Angew. Chem., Int. Ed.*, 2011, **50**, 1164–1167.
34 B. Akdim, R. Pachter and R. R. Naik, *Appl. Phys. Lett.*, 2015, **106**, 183707.
35 C. C. Moser, S. E. Chobot, C. C. Page and P. L. Dutton, *Biochim. Biophys. Acta, Bioenerg.*, 2008, **1777**, 1032–1037.
36 I. Ron, L. Sepunaru, S. Itzhakov, T. Belenkova, N. Friedman, I. Pecht, M. Sheves and D. Cahen, *J. Am. Chem. Soc.*, 2010, **132**, 4131–4140.
37 L. D. D'Andrea and L. Regan, *Trends Biochem. Sci.*, 2003, **28**, 655–662.
38 T. Kajander, A. L. Cortajarena, S. Mochrie and L. Regan, *Acta Crystallogr., Sect. D: Biol. Crystallogr.*, 2007, **63**, 800–811.
39 T. Z. Grove, L. Regan and A. L. Cortajarena, *J. R. Soc., Interface*, 2013, **10**, 20130051.
40 J. López–Andarias, S. H. Mejías, T. Sakurai, W. Matsuda, S. Seki, F. Feixas, S. Osuna, C. Atienza, N. Martín and A. L. Cortajarena, *Adv. Funct. Mater.*, 2018, **28**, 1704031.
41 N. A. Carter and T. Z. Grove, *J. Am. Chem. Soc.*, 2018, **140**, 7144–7151.
42 J. M. Abad, M. Gass, A. Bleloch and D. J. Schiffrin, *J. Am. Chem. Soc.*, 2009, **131**, 10229–10236.
43 Y. Xiao, F. Patolsky, E. Katz, J. F. Hainfeld and I. Willner, *Science*, 2003, **299**, 1877–1881.
44 P. S. Jensen, Q. Chi, F. B. Grumsen, J. M. Abad, A. Horsewell, D. J. Schiffrin and J. Ulstrup, *J. Phys. Chem. C*, 2007, **111**, 6124–6132.
45 T. Guterman, N. L. Ing, S. Fleischer, P. Rehak, V. Basavalingappa, Y. Hunashal, R. Dongre, S. Raghothama, P. Král, T. Dvir, A. I. Hochbaum and E. Gazit, *Adv. Mater.*, 2019, **31**, 1807285.
46 M. T. González, A. Díaz, E. Leary, R. García, M. Á. Herranz, G. Rubio-Bollinger, N. Martín and N. Agraït, *J. Am. Chem. Soc.*, 2013, **135**, 5420–5426.
47 J. Pérez–Juste, L. M. Liz–Marzán, S. Carnie, D. Y. C. Chan and P. Mulvaney, *Adv. Funct. Mater.*, 2004, **14**, 571–579.
48 T. Kajander, A. L. Cortajarena and L. Regan, *Methods Mol. Biol.*, 2006, **340**, 151–170.
49 C. N. Pace, F. Vajdos, L. Fee, G. Grimsley and T. Gray, *Protein Sci.*, 1995, **4**, 2411–2423.
50 X. Liu, M. Atwater, J. Wang and Q. Huo, *Colloids Surf., B*, 2007, **58**, 3–7.
51 T. Z. Grove, L. Regan and A. L. Cortajarena, *J. R. Soc., Interface*, 2013, **10**, 20130051.
52 A. Pena-Francesch, H. Jung, M. A. Hickner, M. Tyagi, B. D. Allen and M. C. Demirel, *Chem. Mater.*, 2018, **30**, 898–905.
53 E. R. G. Main, Y. Xiong, M. J. Cocco, L. D'Andrea and L. Regan, *Structure*, 2003, **11**, 497–508.
54 T. Kajander, A. L. Cortajarena, E. R. G. Main, S. G. J. Mochrie and L. Regan, *J. Am. Chem. Soc.*, 2005, **127**, 10188–10190.
55 S. S. Cohen, I. Riven, A. L. Cortajarena, L. De Rosa, L. D. D'Andrea, L. Regan and G. Haran, *J. Am. Chem. Soc.*, 2015, **137**, 10367–10373.
56 Y. Lu and W. Chen, *Chem. Soc. Rev.*, 2012, **41**, 3594–3623.
57 A. Ursua, L. M. Gandia and P. Sanchis, *Proc. IEEE*, 2012, **100**, 410–426.
58 M. Gilbert and B. Albinsson, *Chem. Soc. Rev.*, 2015, **44**, 845–862.
59 C. Li, C. Xu, D. Cahen and Y. Jin, *Sci. Rep.*, 2019, **9**, 18336.
60 N. A. Carter and T. Z. Grove, *Biomacromolecules*, 2015, **16**, 706–714.